

# WaveFlex: A Smart Surface for Private CBRS Wireless Cellular Networks

Fan Yi<sup>1</sup>, Kun Woo Cho<sup>1</sup>, Yaxiong Xie<sup>2</sup>, Kyle Jamieson<sup>1</sup>

<sup>1</sup>Princeton University, <sup>2</sup>University at Buffalo

## Abstract

We present the design and implementation of **WaveFlex**, the first smart surface that enhances Private LTE/5G networks operating under the shared-license framework in the Citizens Broadband Radio Service frequency band. WaveFlex works in the presence of frequency diversity: multiple nearby base stations operating on different frequencies, as dictated by a Spectrum Access System coordinator. It also handles time dynamism: due to the dynamic sharing rules of the band, base stations occasionally switch channels, especially when priority users enter the network. Finally, WaveFlex operates independently of the network itself, not requiring access to nor modification of the base station or mobile users, yet it remains compliant with and effective on prevailing cellular protocols. We have designed and fabricated WaveFlex on a custom multi-layer PCB, software defined radio-based network monitor, and supporting control software and hardware. Our experimental evaluation benchmarks an operational Private LTE network running at full line rate. Results demonstrate an 8.50 dB average SNR gain, and an average throughput gain of 4.36 Mbps for a single small cell, and 3.19 Mbps for four small cells, in a realistic indoor office scenario.

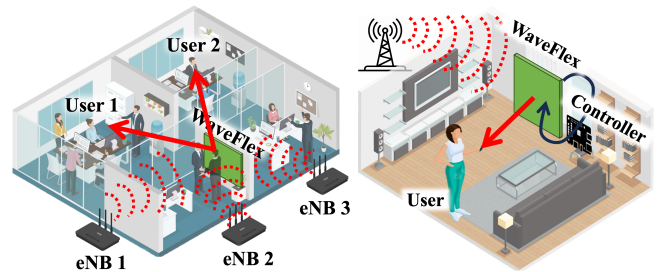
## 1 Introduction

Starting in 1986 with the original design of the predecessor of WaveLAN, and continuing to 802.11 Wi-Fi, wireless networks deployed by enterprises [26,33] and home users have operated on a technology trajectory determined by Wi-Fi hardware, lagging years behind its wireless cellular network cousin.

That status quo is poised to change, however, in the context of the “*Industry 4.0*” manufacturing, retail, and general business trend, and specifically with the advent of locally-managed enterprise 5G deployments [34]. These *Private LTE/5G* cellular networks have recently emerged as a serious competitor that may soon supplant traditional Wi-Fi, due to their superior capabilities. Networks that scale in density to millions of nodes per square mile will support massive Internet

of Things deployment of embedded devices and tags. Networks that scale latency down to milliseconds will support real-time control applications. And networks that scale data rates and capacity to multi-Gbit/second and Tbit/second aggregate throughput per square mile will fully connect users.

Private cellular networks can operate in a number of bands in the radio spectrum, each of which may be accessed under a *licensed*, *unlicensed*, or *shared* basis, according to the relevant government regulations. Shared spectrum access—in the *Citizens Broadband Radio Service (CBRS)* band in the U.S. [13]—is making grassroots, bottom-up deployment of Private 5G networks possible, spurring innovation in a way similar to Wi-Fi in the early 2000s. CBRS offers a unique opportunity for enterprises to deploy Private LTE and 5G networks without needing to acquire expensive, exclusive-use licensed spectrum, even further catalyzing innovation.



(a) Optimizes multi-eNB/multi-user (b) Works independently of the Private 5G networks. network.

**Fig. 1—WaveFlex:** A surface for CBRS Private LTE/5G.

This paper describes the design and implementation of **WaveFlex**, the first practical smart surface that works at full network line rate to enhance the performance of Private LTE/5G<sup>1</sup> wireless cellular networks operating in the CBRS band, and sharing that band with incumbent priority users. Referring to Fig. 1, the shared nature of CBRS band and the complexity

<sup>1</sup>Section 7 compares Private LTE with Private 5G, and outlines WaveFlex’s capabilities and limitations relative to each.

of cellular network imposes new design goals:

- Multi-band:** First, since private cellular networks often comprise multiple base stations (*eNBs/gNBs*) operating at diverse frequencies (directed by the SAS) and in close proximity, WaveFlex requires the versatility to optimize multiple frequency bands at the same time.
- Adaptive:** Second, due to the dynamic sharing nature of the CBRS band, eNB/gNB operating frequencies may vary, especially when higher-tier users enter the network. WaveFlex must therefore be able to adapt its hardware to these changing frequencies.
- Autonomous:** Finally, since WaveFlex is not a part of the existing cellular network infrastructure, it lacks direct access to both eNB/gNB and the mobile user equipment (*UE*). Hence, its control module must function autonomously, without explicit feedback from these entities, yet remaining compliant with prevailing protocols.

Through a novel combination of hardware and software co-design WaveFlex solves each of the foregoing design challenges. WaveFlex’s multi-layer PCB surface design (§5) integrates miniaturized, custom-designed, and tunable channel filters with surface-mounted amplifiers to allow the surface to effectively [50] target multiple CBRS channels simultaneously. Integration of a high-resolution LTE/5G channel monitor with a hardware-software real-time surface controller enables the surface to synchronize with the Private cellular network and adapt its hardware operation at line rate, yet remain independent of (and thus not constrained by) the network itself. Thus, WaveFlex offers deployment advantages, not requiring coordination with nor cooperation with both LTE/5G network equipment vendors and network operators, realizing the first steps toward the vision of smart surfaces for the next generation of cellular networks [6].

Our experimental evaluation (§6) measures the performance gains WaveFlex achieves, versus a private cellular network operating without the system. Microbenchmarks characterize an average SNR gain of 8.50 dB at the physical layer enabled by the surface’s phase shifter and filter circuitry. Additional microbenchmarks then characterize the ability of WaveFlex to time synchronize to a private CBRS network operating at line rate. End-to-end experiments follow, measuring throughput for a single eNB, multiple eNBs, and the ability of the system to adapt in real time to wireless channel and traffic load changes. Results demonstrate WaveFlex is able to achieve an average throughput gain of 4.36 Mbps under a single eNB, and 3.19 Mbps under four eNBs.

## 2 CBRS Primer

The CBRS band for cellular networks is defined as Band 48 by 3GPP, ranging from 3550 to 3700 MHz, as shown in Fig. 2. Although an eNB/gNB may operate anywhere within the CBRS

band, it is typically configured with a center frequency that is a multiple of 10 MHz, and a bandwidth of 10 or 20 MHz.

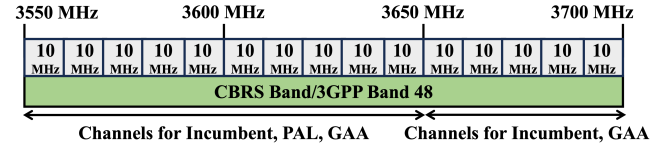


Fig. 2—Frequency plan for operating in the CBRS band.

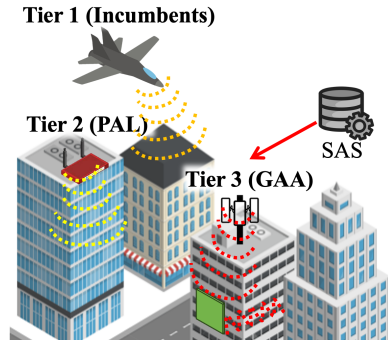


Fig. 3—The CBRS band establishes spectrum sharing rules by user tier (incumbent, priority, and general). Different colors indicate different frequencies used by different user tier.

The CBRS band allocates spectrum to three user *tiers* (see Fig. 3) user system. The top *Incumbent Access Tier*, prioritizes federal operations, ensuring their operations remain interference-free. In the second *Priority Access License (PAL)* tier, entities may obtain licenses via auctions for specific geographies. And in the lowest, unlicensed, *General Authorized Access (GAA)* tier, users may access the CBRS spectrum when users in higher tiers are not. Real-time coordination and allocation of users to these tiers is managed by a *Spectrum Access System (SAS)*. This complexity, however, introduces dynamism to the network, and further, just like Wi-Fi, successful large Private LTE/5G network deployments become the victim of their own success—the radio spectrum becomes crowded with multiple base stations (*eNBs/gNBs*) operating concurrently, each operating on distinct *channels* within the CBRS band, as shown in Fig. 2.

## 3 Related Work

A smart surface, also known as a *reconfigurable intelligent surface (RIS)*, augments—but does not replace—the wireless infrastructure of base stations and mobile users. Many realizations exist, for many different types of wireless networks, but their common goal (and thus far achievement) is to increase the performance of wireless links [5, 24, 27, 44].

Earlier work in the systems and networking community has described the design of smart surfaces with *passive* elements (*i.e.*, elements that do not incorporate an externally

**Table 1— WaveFlex:** comparison to existing surfaces.

Related Works	Network Type	Multi-band	Layer	Auto-nomy	H/W Impl.
[4, 11, 23, 25] [8, 48]	Wi-Fi IoT	Single Single	L1/L2 L1	- -	● ●
[16, 36–38]	-	Dual	L1	-	○
Wall-E [10]	Satellite	Dual	L1/L2	-	-
RF-Bouncer [22]	Wi-Fi	Dual	L1/L2	-	●
CrossFlit [9]	Wi-Fi	Dual	L1/L2	-	●
<b>WaveFlex</b>	<b>LTE/5G</b>	<b>Quad</b>	<b>L1/L2/M</b>	<b>●</b>	<b>●</b>

● = yes; ○ = partially yes; - = no; M = MAC sub-layer

powered amplifier) to improve the performance of Wi-Fi links: LAIA [23], RFocus [4], and ScatterMIMO [11] are three representative examples. These systems have demonstrated compelling performance improvements for Wi-Fi, but do not address the added layers of complexity of the LTE-/5G physical, link, and medium access control sub-layers as summarized in Table 1.

Cao *et al.* design a RIS-assisted medium access control (MAC) protocol for [7] a Wi-Fi-like network using a combination of CSMA and TDMA medium access, similar to IEEE 802.11ac Wi-Fi networks, as do Yuan *et al.* [47] for multiple surfaces. Their efforts do not delve into cellular networks, however, nor do they implement nor experimentally evaluate their concepts end-to-end.

Other work in both the wireless communications and computer systems and networking communities explores the use of *active* elements (*i.e.*, elements that do incorporate an externally powered radio amplifier circuitry). Long *et al.* describe the architecture, compute link budgets, and propose novel optimization algorithms for such systems [28] but stop short of both design above the physical layer and a hardware realization. LAVA [48] realizes these ideas for Wi-Fi and Zigbee networks operating in the 2.4 GHz frequency band but stops short of integrating real-time, line-rate operation into its implementation, and does not address Private LTE/5G cellular networks significantly increased complexity. Zhang *et al.* use a combination of link budgets, modeling, and experimental microbenchmarks to show that in theory, active surfaces can achieve multiplicative gains over passive surfaces [50], yet both stop short of system development and integration with a full-stack cellular network.

Zeng *et al.* [49] investigate the use of a smart surface to harmonize the operation of 5G New Radio and Wi-Fi both operating in an unlicensed (rather than shared-spectrum) frequency band, and propose an alternating optimization to this effect. They present a theoretical performance analysis, but their efforts stop short of both hardware and software design, and operation in shared frequency bands.

LLAMA [8] investigates a smart surface that rotates signal polarization in the context of Internet of Things (IoT) networks operating at 2.4 GHz, and backscatter reflections oc-

curing from tags excited by such networks. VMSscatter [25] designs a MIMO backscatter tag and associated signal processing algorithms. While more complex than Wi-Fi *per se*, these networks are qualitatively simpler than the cellular networks we target here.

Dual-band smart surfaces [16, 36, 38] have recently gained attention, but the existing designs have limitations in satisfying at least one of our criteria, namely, simultaneous multi-eNB/-user optimization, operation over more than two frequency bands, and the absence of explicit feedback from the receiver end as shown in Table 1. Wall-E [10] introduces a dual-band metasurface operating at two Ku bands (*e.g.*, 10/15 GHz) for satellite networking, but this work stops short of hardware design and presents a theoretical performance analysis only with one user. RF-Bouncer [22] investigates a smart surface working at two ISM bands (*e.g.*, 2.4/5 GHz) to expand indoor wireless coverage. However, this work falls short of physical and link layer design and requires an explicit feedback from the receiver to control the surface. Likewise, Chen *et al.* [9] introduces a dual-band metasurface for sub-6GHz and mmWave, but it requires the signal measurement from the receiver to configure the surface. Also, its operating frequencies differ by more than 20 GHz, which poses a less demanding design challenge than our work due to low coupling. Saeidi *et al.* [37] explores frequency-diverse leaky-wave antennas for one-shot detection of multiple wireless nodes, but this work does not integrate with the real-time system.

## 4 Design

We begin by detailing WaveFlex’s architecture in Section 4.1. Section 4.2 describes WaveFlex decoder, which enables WaveFlex’s autonomy. Section 4.3 outlines the WaveFlex controller in the context of a real private cellular network deployment. Section 4.4 describes our multi-channel hardware, emphasizing the tunable filter design and its validation through electromagnetic simulation.

### 4.1 System Overview

Figure 4 presents the architecture of WaveFlex, encompassing the *decoder*, the WaveFlex *controller*, and our frequency-tunable multi-band *surface* itself.

**WaveFlex decoder.** A distinctive feature of WaveFlex is its capability to operate independently without needing explicit information from the SAS, *User Plane Function (UPF)*, or Access and Mobility Management Function (AMF) in the core. Instead, WaveFlex monitors these components of the cellular network by wirelessly monitoring the control plane traffic between the eNB and UE. Keeping in step with the time schedule of the cellular network, the WaveFlex decoder synchronizes with the eNB, and decodes granular, millisecond-level *Downlink Control Information (DCI)*. The decoded

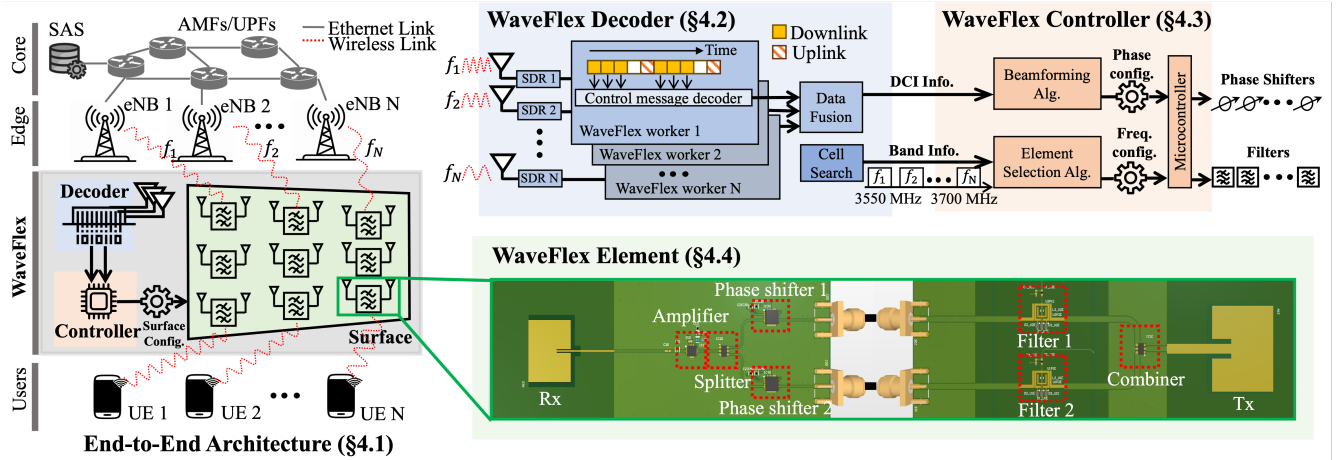


**Fig. 4—WaveFlex architecture overview:** The **decoder** monitors a private cellular network’s operation and synchronizes the system to that network, the **controller** optimizes the surface’s configuration using data from the decoder, and the **surface** amplifies, filters, and modulates ambient network transmissions.

DCI is sent to the WaveFlex controller for subsequent processing.

**WaveFlex controller.** Based on the received DCI, the WaveFlex controller runs a beamforming algorithm and an element selection algorithm to calculate appropriate phase and filter configurations, respectively, which are subsequently sent to the microcontrollers for real-time adjustments.

**WaveFlex surface.** The WaveFlex surface (Figure 4) consists of a series of amplified unit elements, the circuitry of which is illustrated in the lower right of the figure. Each unit element operates independently on each of two CBRS channels (*cf.* §2), as described in Section 4.4. An integrated microcontroller applies phase and filter configurations to phase shifters and custom tunable filters, as instructed by the WaveFlex Controller.

## 4.2 Decoder Design

The WaveFlex decoder performs two functions. It first searches for all nearby private LTE eNBs within CBRS band. Subsequently, the decoder synchronizes with the detected eNBs, decode their control channel to extract DCI. The list of eNBs and extracted DCI is then relayed to the WaveFlex controller for filter control and beamforming phase control, respectively.

**Cell search.** The WaveFlex decoder executes cell search to identify eNBs within CBRS band, which involves traversing the CBRS band and attempting to detect LTE synchronization signals and decode broadcast channels. Given this, the WaveFlex decoder employs a step size of 10 MHz for cell search. If the decoder loses an eNB’s signal due to eNB operating frequency changes, it promptly reinitiates the cell search to

reacquire the eNB’s frequency.

**LTE TDD control channel decoder.** Prior works [21, 45] have demonstrated the feasibility of an external entity decoding the control channel to extract DCI. We design a decoder tailored for Time Division Duplex (TDD), which is the duplexing mode of CBRS band private LTE network. TDD operates by segmenting time into periods, where some periods dedicated for downlink data transmissions and others for uplink.

To decode the TDD control channel, we first determine the arrangement of uplink (U), downlink (D), and special (S)<sup>2</sup> subframes within a frame. We show an example *frame structure configuration* of LTE TDD in Figure 5.<sup>3</sup> Within each frame, the network shifts from downlink to uplink in subframes two and seven.

The frame structure configuration information is carried in *System Information Block 1 (SIB1)*, which occurs every 20 ms and is broadcasted in plain text. The WaveFlex decoder first decodes SIB1 to acquire the frame structure configuration, and based on this information, decodes the control channel for downlink subframes and special subframes, skipping uplink subframes, since DCI is located only in downlink and special subframes. In addition to message decoding, the WaveFlex decoder also computes per-subframe *Reference Signal Received Power (RSRP)* by utilizing the reference signal transmitted within each subframe, regardless of whether there is data transmission within that subframe or not.

<sup>2</sup>S subframes contain downlink and uplink pilot time slots for reference signals, guard periods for tolerance to synchronization uncertainty.

<sup>3</sup>We show one of seven possible frame structure configurations (the configuration of our CBRS eNB)—our system generalizes to others.

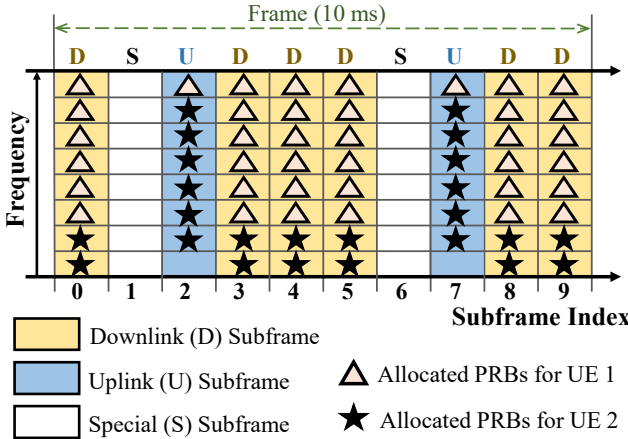


**Fig. 5—CBRS frame structure configuration**, which reflects time-division duplex operation, designating certain *subframes* within a 10-millisecond frame to carry downlink (D) or uplink (U) data traffic to one or more UEs. Special (S) subframes contain reference information for PHY operation.

### 4.3 Controller Design

Using the WaveFlex decoder, the WaveFlex controller calculates optimal phase shifter and filter configurations of each element to maximize network throughput.

#### 4.3.1 Traffic Scheduling in TDD CBRS

The TDD nature of CBRS networks imposes challenges on the design of the WaveFlex controller. First, while downlink traffic demand typically exceeds uplink demand by a ratio of  $2\text{--}3\times$  [46], there is variation between UEs and in time, and so uplink (as well as downlink) traffic must be made reliable in order to facilitate the flow of downlink traffic. Second, when multiple UEs are active, the RAN will schedule different UEs in different subframes, and so WaveFlex must apply different phase shifts to optimize different subframes, at millisecond time granularities. Referring again to the CBRS frame structure (Fig. 5) the eNB switches from downlink to uplink in subframes two and seven. The controller needs to synchronize with the eNB and modulate the phase shifts that it applies to the surface in order to keep pace with the CBRS frame structure link direction.

The time-switched nature of TDD places a precise synchronization requirement between the WaveFlex controller and the eNB. The primary objective is to align the switching of phase configurations in each subframe with the respective downlink and uplink traffic schedules. To address the synchronization problem, our strategy centers on monitoring the periodic pattern of RSRP changes, as shown in Fig. 6. When the WaveFlex controller's element switching pattern is synchronized with the LTE TDD schedule (Fig. 6(a)), we observe a periodicity matched to the TDD schedule as the active transmitter (eNB or any UE) in the schedule changes,

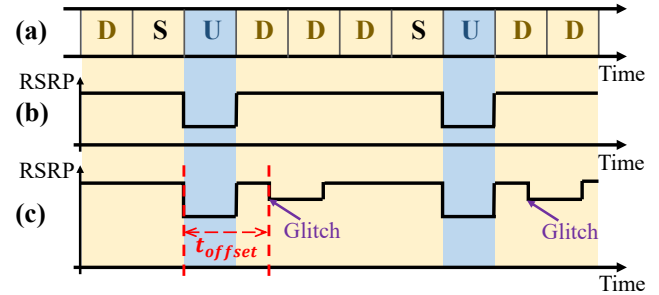


**Fig. 6—Operation of WaveFlex's time synchronization algorithm:** (a) frame structure; (b) synchronized state; (c) unsynchronized state.

as shown in Fig. 6(b).

When the WaveFlex controller's element switching pattern is instead offset by an amount  $t_{\text{offset}}$  from the LTE TDD schedule, we instead observe brief changes in the RSRP curve, as shown in Figure 6(c), where the labeled *glitches* are caused by the mismatch between the downlink/uplink phase configuration transitions of the surface and the (correct) TDD schedule of the eNB. By analyzing the positions of the two periodic RSSI changes, the WaveFlex controller estimates  $t_{\text{offset}}$ , and adjusts its schedule by  $-t_{\text{offset}}$  to converge towards alignment with the network's TDD schedule.

#### 4.3.2 Blind Beamforming Algorithm

To introduce the WaveFlex beamforming algorithm, we start with the description of the algorithm under ideal conditions with only a single UE and a single eNB. We then extend our algorithm to cover multiple UEs and multiple eNBs.

Our algorithm uses *blind-beamforming*, to run without *Channel State Information (CSI)*, [19, 42, 43]. Suppose we have  $K$  elements in the smart surface, and the phases of the  $K$  phase shifters are

$$\boldsymbol{\theta} = [\theta_1, \theta_2, \dots, \theta_K]^T. \quad (1)$$

The blind beamforming algorithm searches for the optimal  $\boldsymbol{\theta}^*$  that maximizes the channel condition:

$$\boldsymbol{\theta}^* = \underset{\boldsymbol{\theta}}{\operatorname{argmax}} M(\boldsymbol{\theta}) \quad (2)$$

where  $M$  (defined below) characterizes the quality of the channel between the transceivers. Blind beamforming solves the problem via an iterative search: it applies a random perturbation  $\delta[n]$  at the  $n^{\text{th}}$  iteration:

$$\boldsymbol{\theta}[n] = \boldsymbol{\theta}[n-1] + \delta[n], \quad (3)$$

where  $\boldsymbol{\theta}[n]$  are the phase settings in the  $n^{\text{th}}$  iteration, repeating the above process until convergence.

**Characterizing cellular channel quality.** WaveFlex's controller works independently without direct feedback from

eNB or UE. Consequently, it cannot directly query the UE for standard channel quality metrics such as the reference received signal power (RSRP), signal to noise ratio (SNR), or CSI. However, we observe that the eNBs implement a bitrate adaption algorithm that adjusts the modulation and coding rate to cope with the quality of the channel between the UE and the base stations, making this rate an excellent proxy for assessing cellular channel conditions. More importantly, the eNB broadcasts the rate index and it is thus decodable by the WaveFlex decoder. The WaveFlex decoder serves as a sniffer to decode the bit rate the eNB broadcasts, and calculates the physical data rate  $R_w$ , an estimate of the greatest number of bits that can be transmitted over one physical resource block without causing errors.

Given the inherent variability of the estimated data rate, we adopt an average rate  $\bar{R}_w$  spanning a preset number of subframes to mitigate the influence of bit rate index fluctuations:

$$\bar{R}_w = \frac{\sum_{i=1}^{N_{sf}} R_w^i}{N_{sf}}, \quad (4)$$

where  $R_w^i$  denotes the rate of the  $i^{th}$  subframe, and  $N_{sf}$  represents the number of subframes used for the averaging process. We use this averaged rate  $\bar{R}_w$  as the optimization target for a single UE scenario:

$$M_{single}(\theta) = \bar{R}_w(\theta). \quad (5)$$

Combining Eqs. (2) and (5), we search for the optimal  $\theta$  that maximizes channel quality  $M_{single}(\theta)$ .

**Extension to multiple UEs.** The blind-beamforming algorithm simultaneously optimizes the channel conditions for multiple UEs. To ensure fairness among UEs, we introduce a channel condition metric tailored for the multi-UE context, which is expressed as:

$$M_{multi} = \frac{\sum_{j=1}^{N_{UE}} \bar{R}_w(j) \times N_{PRB}(j)}{\sum_{j=1}^{N_{UE}} N_{PRB}(j)}, \quad (6)$$

where  $\bar{R}_w(j)$  represents the averaged rate of the  $j^{th}$  UE, and  $N_{PRB}(j)$  corresponds to the summed number of PRBs allocated to the  $j^{th}$  UE in  $N_{sf}$  consecutive subframes.

**Mobility.** As illustrated in Equation 2, the iterative search process maintains a historical record of the highest channel quality value, denoted as  $M_{MAX}$ . This value serves as a benchmark for iteratively searching phase configurations to optimize the channel condition. However, in a dynamic environment,  $M_{MAX}$  expires when wireless channel changes, necessitating a mechanism to detect and react to such channel changes.

We use consecutive negative feedbacks as a sign of possible channel change. Once the number of consecutive negative feedbacks achieves a pre-defined threshold,  $N_{nf}$ , WaveFlex

reconfigures phase settings that corresponds to  $M_{MAX}$ , and then measure the channel quality again, which obtains  $M_{new}$ . If  $M_{new}$  is smaller than  $M_{MAX}$ , WaveFlex identifies that a channel change event happens, and then resets its beamforming parameters, including  $M_{MAX}$ , and  $\theta[n]$ . Our experimental results in Section 6.3.3 demonstrate that this mechanism is able to cope with changes in the wireless channel, even in mobile cases.

### 4.3.3 Multiple-eNB element selection algorithm

The two-way element design naturally fits in with the two-eNB scenario. For scenarios involving more eNBs, we use a greedy search based element selection algorithm to assign elements to the eNBs. Initially, to ensure fairness among eNBs, we evenly and randomly assign the  $K$  elements to the  $N_{eNB}$  eNBs and start running the beamforming algorithm. After the beamforming converges, we record the channel quality  $M$ . We then perturb the element selection by choosing a handful of elements to alternate eNBs while keeping the number of elements assigned to each eNB unchanged. Following another beamforming convergence, the updated channel metric  $M$  is compared against its predecessor. Favorable allocations are retained, while detrimental ones are discarded.

This iterative procedure is maintained until a stable solution is achieved or until there's a shift in the eNB operating frequencies. To accommodate the dynamism in eNB frequencies, the greedy search is reinitialized based on the updated eNB count  $N_{eNB}$ .

## 4.4 Hardware Design

CBRS networks' design shapes the goals of WaveFlex's hardware design, which we illustrate in Fig. 7:

1. **Frequency tunability:** Private CBRS networks generally involve multiple eNBs working on different *channels*, i.e. over non-overlapping frequency ranges. To cope with the dynamics in those operating channels, WaveFlex's hardware must be flexible to adjust its operating frequency.
2. **Concurrent cross-channel isolation:** Further, in a multi-eNB network with concurrent, unsynchronized TDD operation at each eNB, WaveFlex's hardware must help each channel, while not hindering others.

The WaveFlex *unit element* consists of two *patch antennas* that receive and transmit signal respectively, one *phase shifter* to control and adjust the transmitted signal phase, an *amplifier* to boost the output signal level, and one *pass-band filter* to achieve our goals of tunability and isolation, as illustrated in Fig. 8.

To facilitate multi-channel operation, we integrate two single-channel elements into a unified multi-channel element,

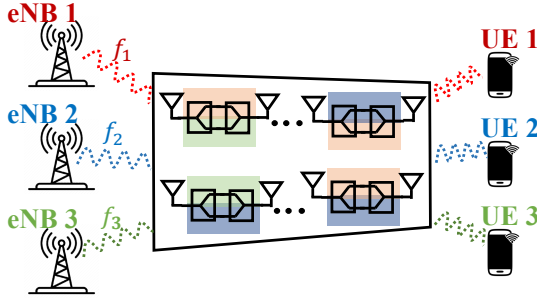


**Fig. 7—Multi-channel operation goal:** different elements affect different CBRS channels independently.

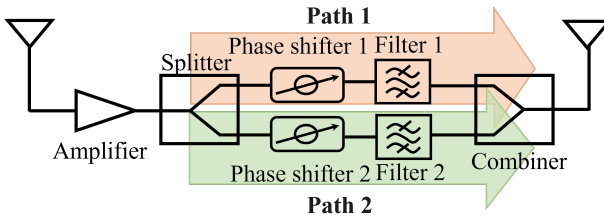


**Fig. 8—Circuit schematic of the WaveFlex unit element.**

as illustrated in the figure. A two-way power splitter-combiner divides the received signal and directs each copy into a respective phase shifter and filter. The signals produced by the two filters are subsequently recombined using another splitter-combiner. Such a configuration enables each single-band unit element to independently modulate the signal phase and tune the two respective operating frequencies of each band-pass filter. Our steep roll-off microstrip filter minimizes cross-talk between the two signal paths residing on the same board.

#### 4.4.1 WaveFlex’s filter design

Our filter design goals are as follows: (1) We require a *band-pass* filter that, for each of the two signal paths traversing the unit element, allows the frequency range of a single CBRS channel that the controller designates (the *pass-band*) to pass through that path with minimal loss, while blocking to a large degree frequencies even minimally outside of that same range. This allows the path to help the channel of interest without negatively impacting other, possibly adjacent CBRS channels (see §2 on p. 2). (2) Our filter must permit agile adjustment of the pass-band to accommodate the dynamic nature of the CBRS frame structure (see Fig. 5 on p. 5). (3) We require a filter that is cost-effective so that the WaveFlex surface can scale up to large unit element counts, for a realistic deployment.

We use dual-mode microstrip filter [17, 18] to design our band-pass filter, which offers advantages such as space conservation, and cost-effectiveness. To meet our requirements of arbitrarily tuning our operating frequencies, we augment the dual-mode microstrip filter with varactors [18, 41]. The varactor is a voltage-dependent capacitor, by applying voltage

on it, we are able to change its capacitance, which affects the filter’s operating frequency.<sup>4</sup> We detail the design of the tunable filter and the derivation of its dimension parameters in Appendix A and Appendix B.

#### 4.4.2 Link Budget

To understand the fundamentals of WaveFlex’s hardware effectiveness and place our later empirical results into context, we derive a link budget of a CBRS network using WaveFlex. When a signal transmitted by the base station travels distance  $d_b$  to reach the WaveFlex element, the signal loss it experiences can be calculated according to the free space path loss:

$$L_{be} = \left( \frac{4\pi d_b}{\lambda} \right)^2 \quad (7)$$

where the  $\lambda$  is the wavelength of the signal. The signal then be received by the receiving antenna, going through all the physical components on the element, and then transmitted again by the transmitting antenna of the element. We characterize the signal gain  $G_{ele}$  after going through one element as:

$$G_{ele} = G_{rx} + G_{tx} + G_{amp} - L_{split} - L_{comb} - L_{phase} - L_{filter} - L_{line} - 3 \quad (8)$$

where  $G_{rx} = 2.46$  dB,  $G_{tx} = 2.46$  dB, and  $G_{amp} = 16.65$  dB are the gain of the transmitting antenna, receiving antenna and the power amplifier. The  $L_{split} = -0.64$  dB,  $L_{comb} = -0.64$  dB,  $L_{phase} = -2.5$  dB,  $L_{filter} = -5$  dB, and  $L_{line} = -1$  dB represent the loss introduced by the signal splitter, signal combiner, phase shifter, the filter and the transmission line of the element. The three dB loss represents the signal loss introduced by the splitting operation. Therefore, the signal emitted by the element undergoes an additional signal loss before reaching the UE. This signal loss is determined by the distance between the UE and the element  $d_u$  and can be calculated as follows:

$$L_{eu} = \left( \frac{4\pi d_u}{\lambda} \right)^2 \quad (9)$$

Therefore, the total loss of a signal that travels through the WaveFlex element before reaching the UE is:

$$L_{ele} = G_{ele} - L_{be} - L_{eu}. \quad (10)$$

Assuming the transmission power of the base station is  $P_b$ , the power loss of the environment path is  $L_{env}$ , and there are  $K$  WaveFlex elements in the smart surfaces, after perfectly adding the signal of the environment path and the signals from

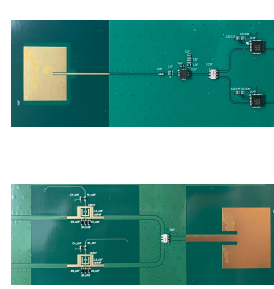
<sup>4</sup>This relationship stems from how electrical signals interact with capacitance: capacitance determines how quickly the filter reacts to incoming signals, and this reaction speed correlates directly with the filter’s resonant frequency.



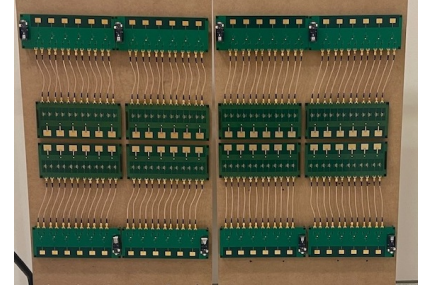
**(a)** USRP X310 (*upper*); Ser-comm cell (*lower*).



**(b)** Arduino controller (*upper*); DAC (*lower*).



**(c)** Receive-half (*upper*); transmit-half (*lower*) custom PCB unit elements.



**(d)** The integrated prototype 48-element, one sq. meter WaveFlex surface deployed on a temporary wall.

**Fig. 9— Hardware implementation:** WaveFlex combines commodity Private LTE and electronics hardware with custom multi-layer PCBs design into an integrated system.

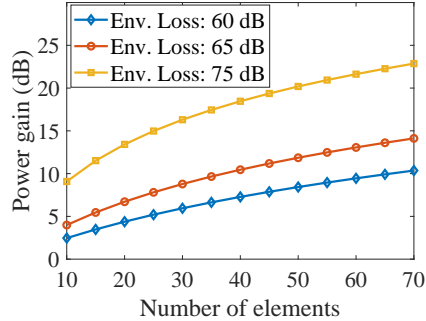


**Fig. 10— The received signal power gain in theory:** the curve is obtained by adjusting number of elements and environment signal loss.

all  $K$  elements, the gain  $G_s$  of such a smart surface is given as:

$$G_s = db \left( \frac{N \cdot db^{-1}(P_b - L_{ele})}{db^{-1}(P_b - L_{env})} \right) \quad (11)$$

where the operation  $db(\cdot)$  represent transforming the amplitude into power in dB and the operation  $db^{-1}(\cdot)$  represents the reverse operation of  $db(\cdot)$ . We have depicted the achieved gain as a function of the number of WaveFlex elements in Fig. 10. It is evident from the plot that the signal gain exhibits a linear increase with the number of elements increases. Moreover, when the environmental path experiences greater signal loss, WaveFlex demonstrates its ability to substantially amplify the signal strength, resulting in even higher gains.

## 5 Implementation

**Surface.** Our WaveFlex surface integrates components on custom multi-layer PCBs, as shown in Figure 9. The surface has 48 elements in total, with a surface area of  $119 \times 76 \text{ cm}^2$ . We use SCN-2-35+ splitter-combiner [32] and TSS-53LNB3+ low noise bypass amplifier [31] from Mini-Circuits in our unit

elements (Fig. 9(c)). We employ Macom MAPS-010144 four-bit phase shifters [29] and an Arduino MKR Wi-Fi 1010 [3] to control the phase of WaveFlex elements at a granularity of  $\pi/8$  (Fig. 9(b)). Our tunable filter is depicted in Figure 9(c) (*lower*). For tunable filter control, we use 40-channel AD5370 DACs from Analog Devices [2] to apply variable bias voltages ranging from 2 to 6 V to Macom MAVR-011005-12790T varactors [30].

**Decoder.** The WaveFlex decoder is modified from NG-Scope [45] to ensure its compatibility with LTE TDD. We pair a laptop with several USRP B210s [12] to execute the WaveFlex decoder (Fig. 9(a) (*upper*)), where each USRP is decoding a distinct eNB to extract DCI. The extracted DCI provides input to our control program, coded in C. This program produces the requisite phase and filter configurations, which are then dispatched to the Arduino microcontrollers and DACs, to adjust the elements' phase shifter and filter.

**Experimental testbed.** We build a real Private LTE network in the CBRS band using a Sercomm *Indoor Enterprise* CBRS Small Cell [39] and the *Aether* core network software [1, 35], shown in Fig. 9(a) (*lower*). The network uses the Google SAS [15] to configure the operating channel of its eNBs.

## 6 Evaluation

In this section, we evaluate the performance of our WaveFlex implementation. We first introduce our evaluation methodology, and then present microbenchmarks evaluating the system under diverse conditions (§6.2). We then demonstrate WaveFlex's end-to-end performance in a real Private LTE network deployment, including a performance evaluation under dynamic conditions, including changes in mobility and traffic demand (§6.3).

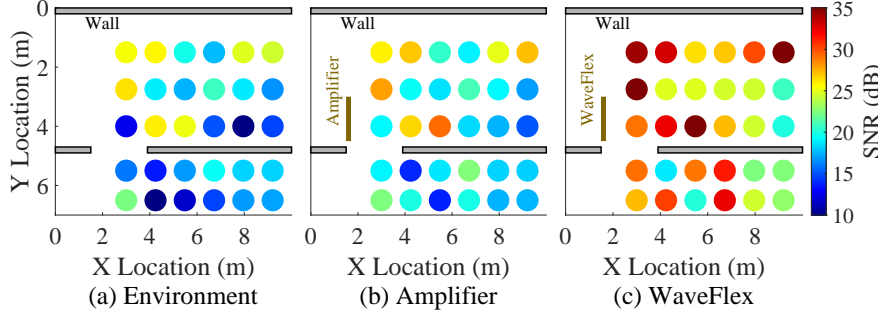


**Fig. 11—SNR map** at 30 locations under three scenarios: (a) the environment alone, (b) the environment with amplifiers on, (c) WaveFlex.

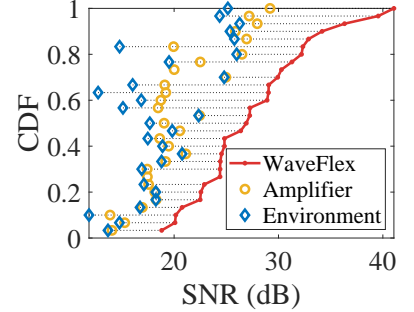
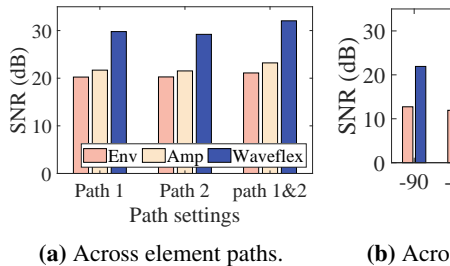
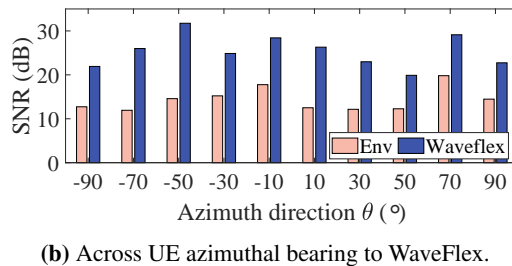


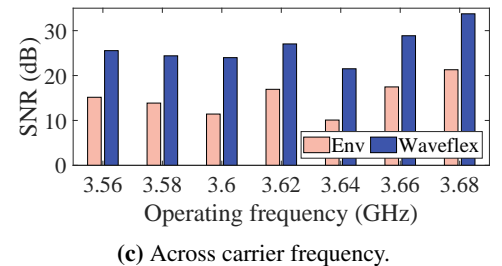
**Fig. 12—Distribution of SNR** across 30 locations.



(a) Across element paths.



(b) Across UE azimuthal bearing to WaveFlex.



(c) Across carrier frequency.

**Fig. 13—Microbenchmark SNR measurements** stratified by element path, azimuthal angle, and carrier frequency.

## 6.1 Experimental Methodology

**Microbenchmark experiments.** For our filter measurement microbenchmarks, we use the Ansys HFSS simulation software package and a Keysight E5063A Vector Network Analyzer (VNA) [20]. For our SNR measurement microbenchmarks, we utilize two laptops equipped with USRP X310s, running SRS-ENB and SRS-UE, as the eNB and UE, respectively [14]. By default, the eNB operates at a frequency of 3.58 GHz.

Our evaluation metric for WaveFlex’s physical layer performance is the *Signal-to-noise ratio (SNR)* at the UE side. We establish a baseline by measuring the SNR in the absence of WaveFlex. Additionally, we take a second baseline by powering-on our surface amplifiers, but without executing the WaveFlex controller to optimize performance. We evaluate WaveFlex’s performance by comparing SNR when executing WaveFlex, to the SNR collected from these two baselines.

**End-to-end experiments.** We conduct end-to-end communication experiments on the testbed described in Section 5. For the UE setup, we connect a Sercomm CBRS USB Dongle to a laptop [40]. Our experiments involve four eNBs and four UEs in total. To decode DCI from four eNBs simultaneously, we connect four USRP B210s to a laptop to run the WaveFlex decoder code. We use the throughput measured at the UE side as the primary metric for these experiments.

## 6.2 Microbenchmark Experiments

In this section, we evaluate WaveFlex’s effectiveness in improving SNR under different conditions, to discern the source of improvements.

### 6.2.1 Performance under single eNB

**Performance across locations.** We fix the locations of the WaveFlex surface and eNB, and measure the SNR at 30 different locations to evaluate the SNR improvement of WaveFlex. As shown in Fig. 11, we perform the experiment in an office scenario of area  $10 \times 7 \text{ m}^2$ . The eNB is located at the left side of the surface, with a distance of five m from the surface. We vary the locations of the UE (indicated by circles in Fig. 11) to cover diverse locations in our indoor office, varying distance and wall penetration.

At each location, the experiment is conducted 20 times. We calculate the average SNR over the 20 measurements and plot them in Fig. 11. The figure shows results under three scenarios, without the WaveFlex surface, enabling amplifiers but without executing the WaveFlex controller, and enabling amplifiers and executing the WaveFlex controller. From this figure, we can observe that in general WaveFlex is able to provide higher SNR improvements for close UEs. Compared with baseline, WaveFlex improves SNR by 9.12 dB for the 15 closer locations, and improves SNR by 7.87 dB for the 15 farther locations on average. For the ten through wall locations, WaveFlex can achieve an improvement of 8.60 dB. Com-

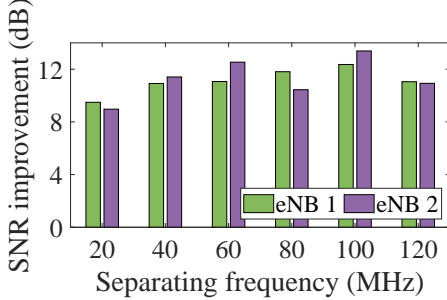


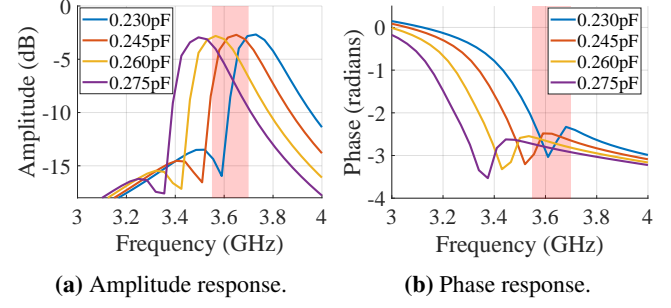
**Fig. 14**—WaveFlex’s SNR improvement of two eNBs versus different eNB carrier frequency separations.

paring Fig. 11(b) and Fig. 11(c), we note that even though the amplifiers are able to achieve high SNR at some locations, WaveFlex outperforms the amplifier case at all locations. Fig. 12 shows the CDF distribution of received SNR across 30 locations. On average, WaveFlex outperforms the amplifier case by 7.02 dB.

**Performance across azimuthal bearing.** We measure WaveFlex’s efficacy under different azimuthal bearings of the UE to the surface itself. We separate the eNB and the WaveFlex surface by 5 m, and maintain the distance between the surface and the UE to 1 m. We vary UE locations to change the UE to surface azimuthal angle from  $-90^\circ$  to  $90^\circ$  with a step size of  $20^\circ$ . Fig. 13(b) presents the average SNR with different azimuth directions with and without the WaveFlex surface. We can see that WaveFlex enhances SNR by 11.05 dB on average across the entire azimuth range. WaveFlex’s lowest improvement in this experiment is 8.26 dB, which happens when at a  $90^\circ$  bearing.

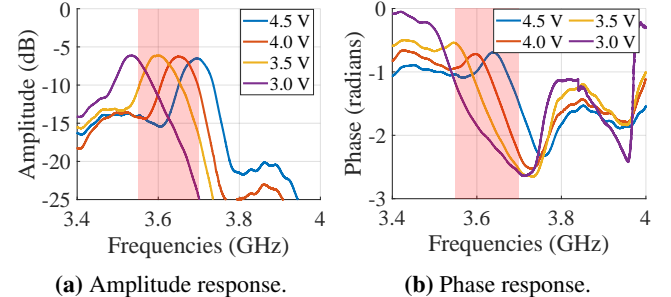
**Performance across element paths.** As introduced in Section 4.4 on p. 6, our unit element comprises two signal paths. We fix the locations of the eNB, the surface, and the UE, and measure the received SNR when only enabling Path 1, only enabling Path 2 and enabling both Path 1 and Path 2. Results are shown in Fig. 13(a): compared to baseline, WaveFlex achieves a similar SNR improvement of 9.55 dB and 8.94 dB with only Path 1 and only Path 2, respectively. Enabling both paths, WaveFlex is able to achieve a higher improvement of 10.94 dB, 1–2 dB better than the respective paths individually.

**Performance across carrier frequency.** To validate WaveFlex’s performance across the whole CBRS band, we conduct experiments that tune the carrier frequency of the surface from 3.56 GHz to 3.68 GHz, with a step size of 20 MHz. We present the measured SNR with and without WaveFlex, in Fig. 13(c). We observe that WaveFlex enhances the SNR for the entire CBRS band, achieving an average SNR improvement of 11.26 dB.



(a) Amplitude response. (b) Phase response.

**Fig. 15**—Simulation: tunable filter amplitude and phase response under varying varactor capacitances.



(a) Amplitude response. (b) Phase response.

**Fig. 16**—VNA measurement: tunable filter response versus frequency under different bias control voltages.

## 6.2.2 Performance under Multiple eNBs

We use two eNBs in this experiment to demonstrate WaveFlex’s ability to simultaneously optimize multiple channels.

**Performance with different frequency separation.** To investigate how the frequency separation of two eNBs influences WaveFlex’s multi-channel performance, we fix the frequency of eNB 1 at 3.56 GHz, and change the frequency of eNB 2 from 3.58 GHz to 3.68 GHz with a step size of 20 MHz. The SNR improvement of eNBs 1 and 2 is presented in Fig. 14. WaveFlex achieves SNR improvement of 9.49 dB and 8.97 dB for eNB 1 and eNB 2, respectively, when the separating frequency is 20 MHz. At frequency separation exceeding 40 MHz, WaveFlex achieves an average SNR gain of 11.44 dB and 11.74 dB for eNB 1, and eNB 2, respectively.

## 6.2.3 Hardware verification

This section presents simulated and then empirical (VNA-based) results on our filter performance. We begin in simulation—Figure 15 shows filter roll-off of up to 4 dB per 20 MHz and an insertion loss between  $-3.5$  dB and  $-3.75$  dB when tuning the center frequency within the CBRS band. A phase response discontinuity occurs outside of the eNB’s target frequency (20 MHz around the center frequency), and thus does not affect our phase tuning for the target channel.

To demonstrate WaveFlex’s filter response and tunability across the CBRS band, we present our VNA measurements

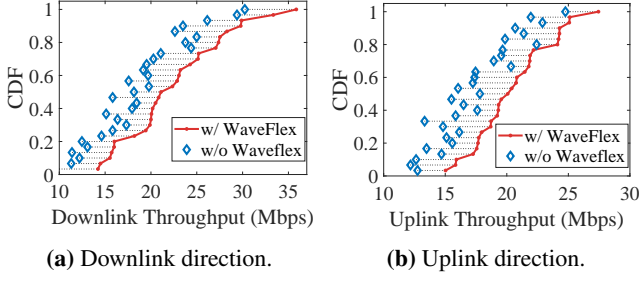


**Fig. 17—End-to-end performance (summary):** distribution of downlink and uplink throughput with and without WaveFlex across 30 locations.

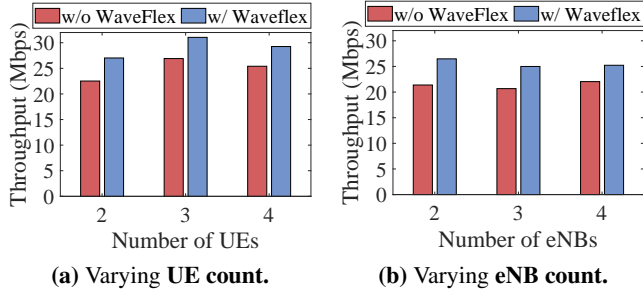


**Fig. 18—End-to-end performance (scaling):** throughput per eNB, varying either UE or eNB count.

from 3.4 to 4 GHz in Fig. 16. By tuning the bias voltage from 3.0 to 4.5 V, we are able to tune the center frequency from 3.55 to 3.7 GHz. From Fig. 16(a), we see that our fabricated filter exhibits an insertion loss of  $-6.1$  dB, exceeding the simulated insertion loss (*cf.* Fig. 15(a)) by 2.5 dB. We ascribe this increased loss to fabrication imperfections, encompassing factors such as transmission line loss and impedance mismatch. The roll-off steepness is 3.23 dB per 20 MHz.

Turning now to empirical phase response, similar to the simulated phase response (*cf.* Fig. 15(b)), we observe in Fig. 16(b) that the phase discontinuity lies outside the eNB’s target frequency range (20 MHz about the center frequency) thus it does not influence our phase tuning capability within the target channel.

### 6.3 End-to-end Performance

In this section, we measure the end-to-end throughput under single eNB and multiple eNB scenarios. We also demonstrate the ability of WaveFlex to adapt in real time to wireless channel and traffic demand changes.

#### 6.3.1 Single eNB throughput

**Single UE.** We fix the location of the WaveFlex surface, 5 m away from the eNB, and measure both downlink and uplink throughput at 30 different locations to evaluate WaveFlex’s

performance in end-to-end private LTE network. We show the CDF distribution of downlink and uplink throughput across 30 locations with and without WaveFlex in Fig. 17. On average, WaveFlex is able to improve throughput by 4.36 Mbps in downlink, and improve throughput by 3.53 Mbps in uplink.

**Multiple UEs.** We change the number of UEs connected to the eNB from two to four, and measure the total downlink throughput of the eNB with and without WaveFlex, to demonstrate WaveFlex’s efficacy: Fig. 18(a) shows that in a two-UE scenario, WaveFlex improves the throughput by 4.50 Mbps on average. The throughput gain is 3.85 Mbps when there are four UEs under the same eNB.

#### 6.3.2 Multi-eNB throughput

In this experiment, we investigate WaveFlex’s capability of simultaneously optimizing for multiple eNBs. We have four CBRS Small Cell eNBs located in two neighboring rooms, and we put the WaveFlex surface in between. We change the number of eNBs from two to four, and present the average throughput per eNB in Fig. 18(b). WaveFlex achieves a high per-eNB throughput gain of 5.10 Mbps with two eNBs, since the two paths design naturally fits in with the two eNB scenario. When increasing the number of eNBs to three and four, WaveFlex’s throughput gain drops to 4.32 Mbps and 3.19 Mbps, respectively. We attribute such drops to the less number of elements allocated to each eNB, when the number of eNB increases.

#### 6.3.3 Mobility

To validate WaveFlex’s performance in mobile scenarios, we show a trace of time-sequenced throughput when the UE moves along a specific route in Fig. 19. We fix the eNB to surface distance to 5 m, and initially the distance between the UE and the surface is 1 m. We then move the UE away from the surface at a constant speed of 0.5 m/s for 10 s. From 2–8 s (the highlighted part in Fig. 19), the UE to eNB line-of-sight (LoS) path is blocked. We move the UE along this route twice to obtain throughput with and without WaveFlex.

During the whole 10 s process, WaveFlex achieves an average throughput gain of 3.95 Mbps, which shows that WaveFlex is able to keep up with environment changes. From 2–8 s, WaveFlex improves the throughput by a higher value 4.58 Mbps, demonstrating WaveFlex’s capability to provide higher throughput gain when the LoS path is blocked.

We present the distribution of throughput with and without WaveFlex when UE moves with different speeds in Fig. 19. For UE speeds of  $v = 0.2, 0.5, 1$  m/s, the average throughput gains achieved by WaveFlex are 4.63 Mbps, 3.95 Mbps, and 3.3 Mbps, respectively. As the UE’s speed increases, the WaveFlex controller detects channel changes more frequently, as depicted in Section 4.3.2. This results in fewer iterations

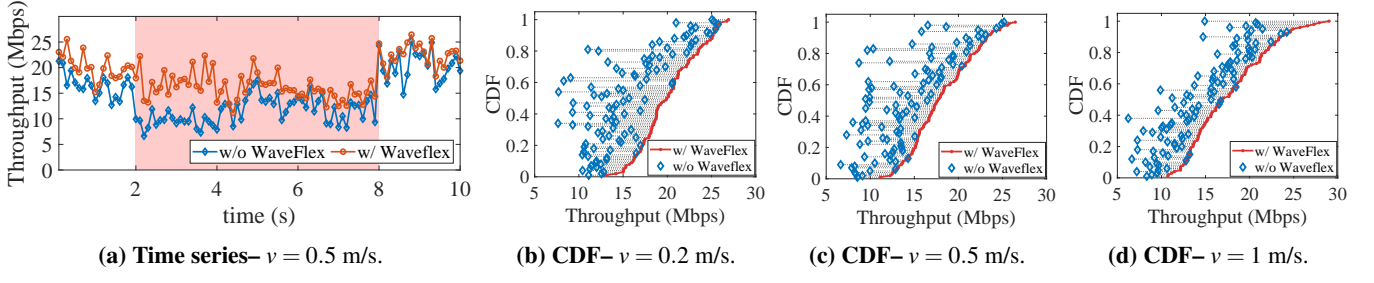


**Fig. 19— WaveFlex’s performance under mobility:** (a) the throughput trace of 10 seconds with and without WaveFlex when UE moves with speed  $v = 0.5$  m/s; (b)-(d) the distribution of throughput with and without WaveFlex when UE moves with speed  $v = 0.2$  m/s,  $v = 0.5$  m/s, and  $v = 1$  m/s, respectively.

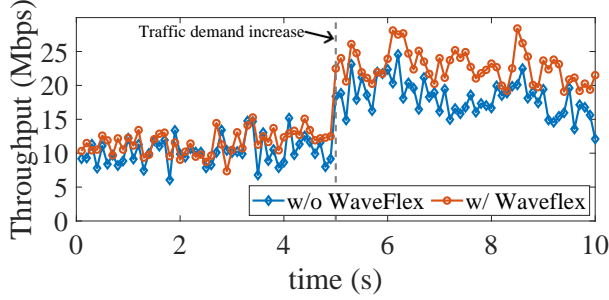


**Fig. 20— WaveFlex’s performance under traffic demand change:** the throughput trace of 10 seconds with and without WaveFlex when UE’s traffic demand changes at the 5<sup>th</sup> second.

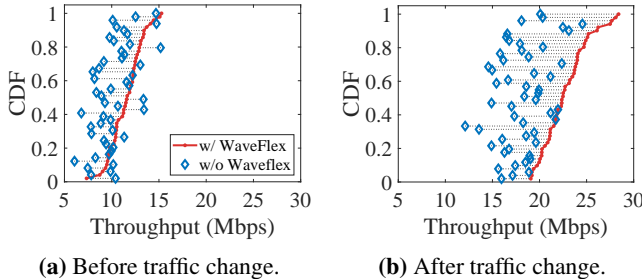


**Fig. 21—** The distribution of throughput with and without WaveFlex before and after the UE traffic demand changes.

for blind beamforming, subsequently leading to a reduced throughput gain.

### 6.3.4 Traffic demand changes

In this experiment, we use *iperf* UDP to control the traffic demand of UE to test WaveFlex’s performance under traffic demand changes. We start by limiting the UE’s traffic demand to 10 Mbps for 5 s, and then increase the traffic demand to 30 Mbps for another 5 s.

We show the time-sequenced throughput when UE’s traffic demand changes with and without WaveFlex in Fig. 20. We also present the throughput distribution of WaveFlex before

and after a traffic demand change in Fig. 21. For the first 5 s, the throughput gain of WaveFlex is 1.38 Mbps, we argue that in this period, the wireless link capacity is enough to support the UE’s traffic even without WaveFlex, because the traffic demand is low. From 5 s to 10 s, WaveFlex improves the throughput by 4.58 Mbps, which proves that WaveFlex is able to identify and react to traffic demand changes.

## 7 Conclusion

We have described the design and practical real-world implementation of WaveFlex, the first smart surface that has demonstrated the capability to enhance the operation of real-world Private LTE networks operating in the CBRS shared spectrum licensing regime. WaveFlex operates autonomously from the core and RAN, easing deployment by obviating the need to interface with cellular providers or even private cellular network system administrators on-site. The autonomous nature of our design opens up new possibilities to incrementally deploy smart surfaces in private CBRS networks, and gives a new direction to the area in general. Also from an engineering perspective, our design breaks new ground for smart surfaces, adapting to shifting traffic demands and the vagaries of the wireless channel in real time.

**Limitations.** Our implementation and evaluation are in a Private LTE network, and we acknowledge that implementation of WaveFlex for Private 5G networks is ongoing and future work. WaveFlex is designed for both Private LTE and Private 5G CBRS networks, which have a slightly different control and data channel formats, but similar overall architecture. WaveFlex is implemented in TDD-mode LTE (as opposed to FDD mode), which the industry is moving towards for 5G New Radio, owing to its superior performance.

## 8 Acknowledgements

This material is based upon work supported by the National Science Foundation under Grant Nos. CNS-2223556 and CNS-2232457 and the Sony Research Award Program.

## References

- [1] Aether: An ONF Project. [\[org\]](#).
- [2] Analog Devices AD5370 40-ch. 16-bit DAC. [\[pdf\]](#).
- [3] Arduino MKR Wi-Fi 1010. [\[pdf\]](#).
- [4] V. Arun, H. Balakrishnan. RFocus: Beamforming using thousands of passive antennas. *USENIX NSDI Symp.*, 1047–1061, 2020.
- [5] E. Basar, M. Di Renzo, J. De Rosny, M. Debbah, M.-S. Alouini, R. Zhang. Wireless communications through reconfigurable intelligent surfaces. *IEEE Access*, 7, 116,753–116,773, 2019.
- [6] E. Basar, H. V. Poor. Present and future of reconfigurable intelligent surface-empowered communications [perspectives]. *IEEE Sig. Proc. Mag.*, 38(6), 146–152, 2021.
- [7] X. Cao, B. Yang, H. Zhang, C. Huang, C. Yuen, Z. Han. Reconfigurable intelligent surface-assisted MAC for wireless networks: protocol design, analysis, and optimization. *IEEE Internet of Things Journal*, 2021.
- [8] L. Chen, W. Hu, K. Jamieson, X. Chen, D. Fang, J. Gummesson. Pushing the physical limits of IoT devices with programmable metasurfaces. *USENIX NSDI Symp.*, 2021.
- [9] L. Chen, B. Yu, J. Ren, J. Gummesson, Y. Zhang. Towards seamless wireless link connection. *Proceedings of the 21st Annual International Conference on Mobile Systems, Applications and Services*, 137–149, 2023.
- [10] K. W. Cho, Y. Ghasempour, K. Jamieson. Towards dual-band reconfigurable metasurfaces for satellite networking. *Proceedings of the 21st ACM Workshop on Hot Topics in Networks*, 17–23, 2022.
- [11] M. Dunna, C. Zhang, D. Sievenpiper, D. Bharadia. ScatterMIMO: enabling virtual MIMO with smart surfaces. *ACM MobiCom Conf.*, 2020.
- [12] The Ettus Research USRP B210. [\[url\]](#).
- [13] FCC. 3.5 GHz band overview. [\[fcc.gov\]](#), 2023.
- [14] I. Gomez-Miguelez, A. Garcia-Saavedra, P. D. Sutton, P. Serrano, C. Cano, D. J. Leith. srsLTE: an open-source platform for LTE evolution and experimentation. *ACM WiNTECH*, 2016.
- [15] Google Spectrum Access System (SAS). [\[url\]](#).
- [16] J. Han, R. Chen. Dual-band metasurface for broadband asymmetric transmission with high efficiency. *Journal of Applied Physics*, 130(3), 2021.
- [17] J.-S. Hong, H. Shaman, Y.-H. Chun. Dual-mode microstrip open-loop resonators and filters. *IEEE Trans. on Microwave Theory and Techniques*, 55(8), 1764–1770, 2007.
- [18] J.-S. G. Hong, M. J. Lancaster. *Microstrip filters for RF/microwave applications*. John Wiley and Sons, 2004.
- [19] S. Jayaprakasam, S. K. A. Rahim, C. Y. Leow. Distributed and collaborative beamforming in wireless sensor networks: Classifications, trends, and research directions. *IEEE Comms. Sur. and Tut.*, 19(4), 2092–2116, 2017.
- [20] E5063A ENA Vector Network Analyzer. [\[url\]](#).
- [21] S. Kumar, E. Hamed, D. Katabi, L. Erran Li. LTE radio analytics made easy and accessible. *ACM SIGCOMM CCR*, 44(4), 211–222, 2014.
- [22] X. Li, C. Feng, X. Wang, Y. Zhang, Y. Xie, X. Chen. Rf-bouncer: A programmable dual-band metasurface for sub-6 wireless networks. *USENIX NSDI Symp.*, 2023.
- [23] Z. Li, Y. Xie, L. Shangguan, R. I. Zelaya, J. Gummesson, W. Hu, K. Jamieson. Towards programming the radio environment with large arrays of inexpensive antennas. *USENIX NSDI Symp.*, 285–300, 2019.
- [24] C. Liaskos, S. Nie, A. Tsoliariidou, A. Pitsillides, S. Ioannidis, I. Akyildiz. A New Wireless Communication Paradigm through Software-Controlled Metasurfaces. *IEEE Comms. Mag.*, 56(9), 162–169, 2018.
- [25] X. Liu, Z. Chi, W. Wang, Y. Yao, T. Zhu. VMscatter: a versatile MIMO backscatter. *USENIX NSDI Symp.*, 895–910, 2020.
- [26] X. Liu, A. Sheth, M. Kaminsky, K. Papagiannaki, S. Seshan, P. Steenkiste. DIRC: Increasing Indoor Wireless Capacity Using Directional Antennas. *Proc. of ACM SIGCOMM*, 2009.
- [27] Y. Liu, X. Liu, X. Mu, T. Hou, J. Xu, M. Di Renzo, N. Al-Dhahir. Reconfigurable intelligent surfaces: Principles and opportunities. *IEEE Comms. Surveys & Tutorials*, 23(3), 1546–1577, 2021.
- [28] R. Long, Y.-C. Liang, Y. Pei, E. G. Larsson. Active reconfigurable intelligent surface-aided wireless communications. *IEEE Trans. on Wireless Comms.*, 20(8), 4962–4975, 2021.
- [29] Macom MAPS-010144 four-bit phase shifter. [\[pdf\]](#).
- [30] Macom MAVR-011005-12790T surface mount GaAs tuning varactor. [\[pdf\]](#).
- [31] Mini-Circuits Low Noise Bypass Amplifier TSS-53LNB3+. [\[pdf\]](#).
- [32] Mini-Circuits Power Splitter/Combiner SCN-2-35+. [\[pdf\]](#).
- [33] R. Murty, J. Padhye, R. Chandra, A. Wolman, B. Zill. Designing High Performance Enterprise Wi-Fi Networks. *Proc. of USENIX NSDI Symp.*, 2008.
- [34] L. Peterson, O. Sunay. *5G Mobile Networks: A Systems Approach*. [\[github\]](#), 2022. License: CC BY-NC-ND 4.0.
- [35] L. Peterson, O. Sunay, B. Davie. *Private 5G: A Systems Approach*. [\[github\]](#), 2022. License: CC BY-NC-ND 4.0.
- [36] D. Rotshild, A. Abramovich. Ultra-wideband reconfigurable X-band and Ku-band metasurface beam-steerable reflector for satellite communications. *Electronics*, 10(17), 2165, 2021.

- [37] H. Saeidi, S. Venkatesh, X. Lu, K. Sengupta. 22.1 thz prism: One-shot simultaneous multi-node angular localization using spectrum-to-space mapping with 360-to-400ghz broadband transceiver and dual-port integrated leaky-wave antennas. *2021 IEEE International Solid-State Circuits Conference (ISSCC)*, vol. 64, 314–316. IEEE, 2021.
- [38] Y. Saifullah, Q. Chen, G.-M. Yang, A. B. Waqas, F. Xu. Dual-band multi-bit programmable reflective metasurface unit cell: design and experiment. *Optics Express*, **29**(2), 2658–2668, 2021.
- [39] Sercomm Indoor Enterprise CBRS eNB. [\[url\]](#).
- [40] Sercomm Indoor Enterprise CBRS UE. [\[url\]](#).
- [41] W. Tang, J.-S. Hong, Y.-H. Chun. Compact tunable microstrip bandpass filters with asymmetrical frequency response. *Proc. of the European Microwave Conf.*, 599–602. IEEE, 2008.
- [42] C.-S. Tseng, C.-C. Chen, C. Lin. A bio-inspired robust adaptive random search algorithm for distributed beamforming. *IEEE ICC Conf.*, 1–6, 2011.
- [43] C.-S. Tseng, J. Denis, C. Lin. On the robust design of adaptive distributed beamforming for wireless sensor/relay networks. *IEEE Trans. on Sig. Proc.*, **62**(13), 3429–3441, 2014.
- [44] A. Welkie, L. Shangguan, J. Gummesson, W. Hu, K. Jamieson. Programmable radio environments for smart spaces. *ACM HotNets Workshop*, 2017.
- [45] Y. Xie, K. Jamieson. NG-Scope: Fine-grained telemetry for NextG cellular networks. *Proc. of the ACM on Measurement and Analysis of Computing Systems*, **6**(1), 1–26, 2022.
- [46] B. Yang, W. Guo, Y. Jin, S. Wang. Smartphone data usage: downlink and uplink asymmetry. *Electronics Letters*, **52**(3), 243–245, 2016.  
doi:<https://doi.org/10.1049/el.2015.3249>.
- [47] J. Yuan, Y.-C. Liang, J. Joung, G. Feng, E. G. Larsson. Intelligent reflecting surface-assisted cognitive radio system. *IEEE Trans. on Comms.*, **69**(1), 675–687, 2021.
- [48] R. I. Zelaya, W. Sussman, J. Gummesson, K. Jamieson, W. Hu. LAVA: fine-grained 3D indoor wireless coverage for small IoT devices. *ACM SIGCOMM Conf.*, 123–136, 2021.
- [49] M. Zeng, X. Ning, W. Wang, Q. Wu, Z. Fei. RIS aided NR-U and Wi-Fi coexistence in single cell and multiple cell networks on unlicensed bands. *IEEE Trans. on Green Comms. and Net.*, **7**(3), 1528–1541, 2023.
- [50] Z. Zhang, L. Dai, X. Chen, C. Liu, F. Yang, R. Schober, H. V. Poor. Active RIS vs. passive RIS: Which will prevail in 6G? *IEEE Trans. on Comms.*, **71**(3), 1707–1725, 2023.

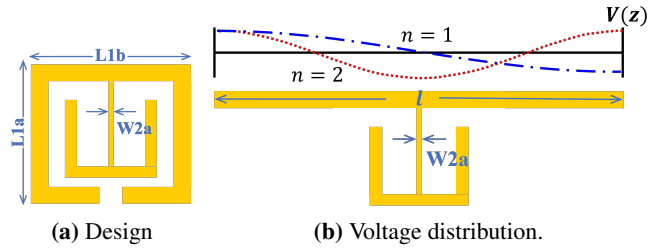


**Fig. 22— Filter design and principle of operation.**

## A Microstrip Filter Design

We design a *microstrip* filter, a low-cost but effective filter that consists of a series of conductive metal traces printed on a PCB dielectric substrate.

The roll-off steepness of such filter depends on its order.<sup>5</sup> A higher-order filter allows a steeper roll-off but increases the design complexity and signal loss. To mitigate this problem, WaveFlex uses a *dual-mode open loop* microstrip filter as shown in Fig. 22(a). Each of the two constituent resonator loops functions as a doubly-tuned resonant circuit, halving the number of required resonators for a higher-order filter [18] and thereby simplifying the filter design.

Figure 22 illustrates the operating principle of our filter. Consider unfolding the outer loop (Fig. 22(a)) into a straight line (Fig. 22(b)). The loop resonates when its length  $l = n \cdot \lambda/2$  where  $n$  is an arbitrary integer, and  $\lambda$  is a wavelength. In Figure 22(b), we visualize the voltage distribution  $V(z)$ <sup>6</sup> across the unfolded resonator when  $n = 1, 2$  (e.g., at its first two resonant frequencies). Since the resonator's two ends have a zero current, the voltage level maximizes at these two locations. Hence, the curvatures of voltage distribution are restricted to two modes.

The first mode is called *an odd mode* with  $n$  being an odd integer. Here, the center of the outer resonator has a zero voltage. Since the resonator cannot be excited at the location of voltage nulls, the voltage does not pass into the inner loop, and the resonance occurs only in the outer loop. The second mode is *an even mode* with even  $n$  and a maximum voltage level at the center. Here, both the inner loading element and the outer loop resonate, giving rise to two separate resonant frequencies. By carefully adjusting the dimensions of the outer and inner loop, we can tune the operating frequencies. We design our resonator such that two resonant frequencies correspond to the edges of the desired pass band. We will further elaborate on our design parameters in Appendix B.

<sup>5</sup>The order of a filter depends on the number of reactive components (e.g., a third-order filter requires at least three components: one capacitor and two inductors, two capacitors and one inductor)

<sup>6</sup>The supply voltage is shared within the resonator loop. The sum of the voltages across the loop is equal to the voltage of the supply.

## B Tunable Filter Dimensions

We present a detailed derivation of tunable filter dimensions. To concurrently and proportionally adjust the resonant frequencies of the odd and even modes by applying a single bias voltage, the tuning rates of both modes must be analyzed. The tuning rate reflects the change in a modal frequency resulting from a variation in the capacitance  $C_v$ . Assuming that when  $C_v$  changes from  $C_{v1}$  to  $C_{v2}$ , the odd-mode frequency shifts from  $f_{01}^o$  to  $f_{02}^o$ , and the even-mode frequency alters from  $f_{01}^e$  to  $f_{02}^e$ . The proportional tuning rate condition can be mathematically represented as,

$$R_t = \frac{f_{02}^o - f_{01}^o}{C_{v2} - C_{v1}} = \frac{f_{02}^e - f_{01}^e}{C_{v2} - C_{v1}}, \quad (12)$$

where  $R_t$  denotes the tuning rate.

The simplified circuit model for the odd and even modes is illustrated in Figure 23.  $Y_o$ ,  $Y_e$ ,  $\theta_o$ ,  $\theta_e$  represent the equivalent admittances and electrical lengths for the transmission line segments in the figure. According to [18], the input admittance for the odd mode is given by,

$$Y_{ino} = j \left( \omega C_v - \frac{Y_o}{\tan \theta_o} \right), \quad (13)$$

and for the even mode, it is,

$$Y_{ine} = j \left( \omega C_v + Y_o \frac{Y_e + Y_o \tan \theta_o}{Y_o - Y_e \tan \theta_o} \right), \quad (14)$$

where  $C_v$  represents the capacitance of the varactors. The resonant frequencies of the odd and even modes can be determined from the following conditions, respectively,

$$\text{Im}[Y_{ino}] = 0, \text{Im}[Y_{ine}] = 0. \quad (15)$$

By examining Equation 13 and Equation 14, it is apparent that the resonant frequency of the even mode can be altered by adjusting  $Y_e$  and  $\theta_e$ , while keeping the resonant frequency of the odd mode unchanged. We solve the equations 12, 13, 14, 15 to obtain  $Y_o$  and  $\theta_o$ ,  $Y_e$  and  $\theta_e$ , that align the tuning rate of the two modes.  $Y_{o/e}$  and  $\theta_{o/e}$  correspond to the width and length of the metal traces, respectively.

In order to ensure that the adjustable range encompasses the CBRS band from 3550 MHz to 3700 MHz, the resolved  $Y_e$  value corresponds to a large inductance value, which equates to a thin loading element that cannot be fabricated. To overcome this issue, we incorporate an inductor  $L_1 = 0.5 \text{ nH}$  in the loading element, as shown in Figure 24.

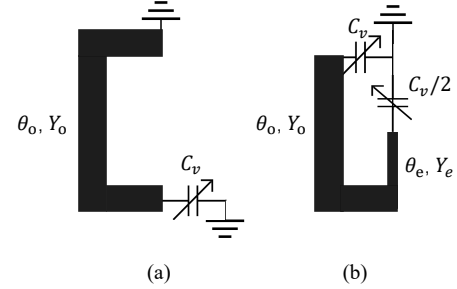


**Fig. 23**—The circuit model of tunable filter: (a) odd mode, and (b) even mode.

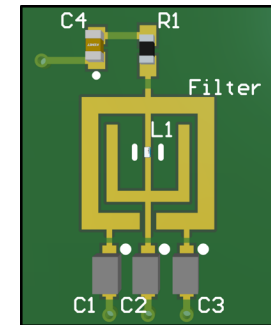


**Fig. 24**—The 3D model of our tunable filter.